

pubs.acs.org/Macromolecules Article

Synthesis and Self-Assembly of Silicon-Containing Azobenzene Liquid Crystalline Block Copolymers

Lin Weng, Mingchao Ma, Chenxiao Yin, Zhi-Xiong Fei, Ke-Ke Yang, Caroline A. Ross, and Ling-Ying Shi*



Cite This: https://doi.org/10.1021/acs.macromol.2c02343



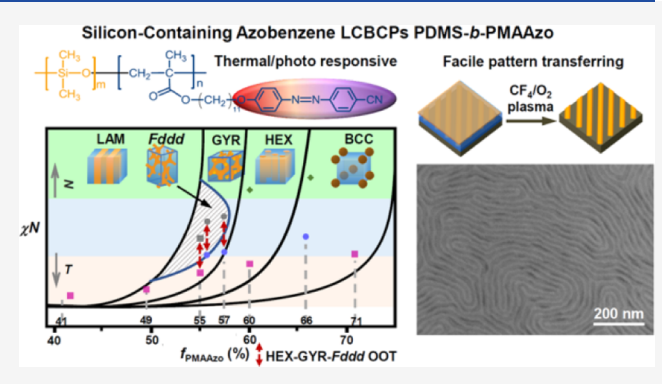
ACCESS I

III Metrics & More

Article Recommendations

s Supporting Information

ABSTRACT: The synthesis and self-assembly of a high interaction parameter silicon-containing liquid crystalline block copolymer (Si-LCBCP) are reported, containing thermally and photo-responsive azobenzene mesogens in the side chains which undergo molecular structural transitions, influencing phase transitions and orientation in the block copolymer. A series of the azobenzene-containing Si-LCBCPs, poly{dimethylsiloxane-b-11-[4-(4-cyanophenylazo)-phenoxy]undecane methacrylate}, were synthesized through atom transfer radical polymerization, and the bulk self-assembly as well as the influence of the liquid-crystalline (LC) phase transition of the LC block on the microphase-separated nanostructure of the BCPs is described. As the volume fraction of the PMAAzo block (f_{PMAAzo}) changes from 41 to 71%, lamellar, double gyroid (GYR),



orthorhombic Fddd network, hexagonally packed cylindrical (HEX), and body centered cubic nanostructures were obtained. When $f_{\text{PMAAzo}} = 55-57\%$, a thermally reversible HEX-GYR-Fddd phase transition induced by the temperature change and LC phase transition was observed. Bulk morphologies are compared with thin-film self-assembly, and pattern transfer into silica nanostructures is demonstrated.

1. INTRODUCTION

Block copolymers (BCPs) have garnered much attention in applications including nanoporous membranes, $^{1-3}$ mesoporous templates, 4 and nanolithography 5,6 due to their capability of yielding various well-defined ordered nanostructures with tunable sizes on the few nm-100 nm length scale. The self-assembly and properties of BCPs depend on the Flory—Huggins interaction parameter (χ), the overall degree of polymerization (N), and the volume fraction f of each block. High- χ low-N BCPs enable the formation of small-size periodic features which are useful for advanced nanotechnology such as nanopatterning and the fabrication of small pore-size filtration membranes. $^{8-10}$

High- χ BCPs consist of two polymer blocks with quite different physical and chemical properties, which is often accomplished by pairing a block incorporating fluorine, carbonate, or silicon with a block such as polystyrene (PS), poly(methyl methacrylate), polyhydroxystyrene, and so forth. A silicon-containing block, for instance PDMS (polydimethylsiloxane), polyferrocenylsilane, or polyoctahedral silsesquioxanes, combined with an organic block such as PS yields a BCP possessing not only high- χ values for strong microphase separation but also native etch contrast for facile pattern transfer. The thin-film self-assembly of silicon-

containing BCPs has been investigated extensively for nanopatterning applications.^{6,11,14–16,19}

Incorporating liquid-crystalline (LC) mesogens into BCPs produces LCBCPs which can form "structure-in-structure" hierarchical morphologies, that is, ordered LC phases within the microphase-separated domains. 20,21 The LC behavior not only enhances the immiscibility or chemical incompatibility between two blocks to increase the tendency for microphase-separation but also offers an effective way to switch the morphologies and orientation of the microphase-separated nanostructures by modulating the alignment of the LC mesogens via changes in temperature, solvents, magnetic field, and light illumination. $^{22-26}$ As an example, LCBCPs can experience diverse order-to-order transitions (OOTs) triggered by the LC phase transition in addition to the temperature-induced OOTs typical for BCPs that are attributed to the temperature-dependent χ . $^{26-30}$ In particular, azobenzene LC mesogens present a photoswitchable configuration change

Received: November 17, 2022



between cis and trans, that is, forming the low-energy trans configuration under visible light or heat treatment but the cis isomer upon irradiation with UV light. Thus, light of different wavelengths can be utilized to manipulate the orientation of azobenzene-containing LCBCPs. $^{32-34}$ For example, the cylindrical morphology of azobenzene photoresponsive LCBCPs can be transformed from random or inplane orientation to out-of-plane vertical alignment under light irradiation. $^{23,35-37}$

In this work, we report the synthesis and morphology of a silicon-containing side-chain azobenzene LCBCP, poly-{dimethylsiloxane-b-11-[4-(4-cyanophenylazo)phenoxy]undecane methacrylate}, which combines the advantages of a high-\(\chi\) value for producing sub-22 nm periodic features, thermal and light-responsive characteristics for morphology control, and good etch contrast for pattern transfer. Although the synthesis method and the phase separation morphologies of similar materials have been studied, ^{37–39} the complete phase diagram remains to be elucidated. For example, Aoki and coworkers demonstrated the photoreorientation of one composition of PDMS-b-PMAAzo.38 Wei et al. prepared a series of PDMS-b-PMAAzo with PDMS wt % from 23.3 to 57.8 to investigate the morphologies after thermal annealing,³ obtaining only lamellar (LAM), spherical, and cylindrical microdomain structures. These BCPs had six methylene spacers between the mesogen and the backbone,³⁹ which is much shorter than the length in our materials (11 spacers). The length of spacers has considerable influence on the properties of azobenzene-containing polymers, including their absorption spectra, ^{40–42} melting temperature, ^{40,43} photo-isomerization, ^{42,44} and especially morphology. ^{41,43,45,46} LC structures consisting of a combination of host and guest LC molecules are promoted in azobenzene-containing BCPs with a longer spacer length.⁴⁵

Here, a series of PDMS-b-PMAAzo with different molecular weights and volume fractions of the LC block were synthesized through atom transfer radical polymerization (ATRP). The bulk phase behavior of the LCBCPs and the influence of temperature and phase transitions of the PMAAzo blocks on the microphase-separated structures were investigated by small-angle X-ray scattering (SAXS) and transmission electron microscopy (TEM) experiments. LAM, gyroid (GYR), hexagonally packed cylindrical (HEX), and body centered cubic (BCC) nanostructures as well as a network with Fddd (orthorhombic space group number 70) symmetry⁴⁷ were obtained. When the volume fractions of the PMAAzo $(f_{\text{PMAAzo}}) = 55-57\%$, a thermally reversible HEX-GYR-Fddd transition was found. Finally, the thin-film self-assembly of HEX morphologies under thermal annealing was studied and the nanostructures were transformed into silicon oxide patterns by plasma etching. This work illustrates the strategy of incorporating thermally and photoresponsive azobenzene LC mesogens into silicon-containing BCPs for morphology control with promise for applications in nanofabrication.

2. EXPERIMENTAL SECTION

2.1. Synthesis of PDMS-*b***-PMAAzo by ATRP.** A series of PDMS-*b***-PMAAzo** BCPs were synthesized by ATRP (Scheme 1) using PDMS-Br as macroinitiators prepared from the hydroxylterminated PDMS. The preparation and characterization of the PDMS-Br macroinitiator and MAAzo azobenzene LC monomer are described in the Supporting Information (Scheme S1 and Figure S1) and Figure 1a. Three PDMS-Br macroinitiators with degrees of

Scheme 1. Synthesis of PDMS-b-PMAAzo Block Copolymers

polymerization of \sim 63, 101, and 180 were used and the corresponding three series of PDMS-b-PMAAzo diblock copolymers (noted as $D_{63}M_n$, $D_{101}M_n$ and $D_{180}M_n$) with different lengths of the PMAAzo block were synthesized by changing the ratio of the macroinitiator to monomer. Figure 1a shows typical ¹H NMR spectra of the MAAzo, PDMS-Br, and the PDMS-b-PMAAzo.

Taking the synthesis of $D_{63}M_{17}$ as a typical example, the monomer $\{11\text{-}[4\text{-}(4\text{-}\text{cyanophenylazo})\text{phenoxy}]\text{undecane} \mod \text{methacrylate}\}$ (MAAzo) (0.52 g, 1.12 mmol), PDMS-Br (0.15 g, 2.24 × 10^{-2} mmol), CuBr (0.0032 g, 2.24 × 10^{-2} mmol), PMDETA (4.6 μ L, 2.24 × 10^{-2} mmol), and chlorobenzene (4 mL) were charged into a Schleck tube. After being stirred and degassed by three freeze—pump—thaw cycles, the tube was sealed under vacuum and subsequently immersed into an oil bath held at 80 °C for 8 h. After the reaction was over, the tube was brought to ambient conditions and in contact with air. The solution was passed through a neutral alumina column to remove copper salts. Finally, the copolymer was precipitated in a large volume of methanol, and then, the precipitates were collected and dried in vacuum overnight. Figure 1a(iii) shows representative 1 H NMR spectra of the PDMS-b-PMAAzo BCPs.

2.2. Annealing Method for Bulk and Thin-Film Samples. The BCP was dissolved in tetrahydrofuran (THF) to prepare a solution of 40 mg/mL, stirred overnight to ensure that the solution was completely mixed, and then, the polymer was dried by evaporating the THF at an ambient temperature. Afterward, the evaporated polymer sample was thermally annealed at 150 °C in a vacuum environment for 2 days.

Solutions of the PDMS-b-PMAAzo BCP were made in toluene with concentration 1.5 wt %. Films with a thickness of 40 nm were obtained by spin-coating on as-received Si substrates and on PDMS-brush functionalized Si substrates. The films were thermally annealed at 140–180 °C under vacuum (20 Torr) for 48–72 h.

2.3. Characterization Methods. The chemical structures and molecular weights of PDMS-*b*-PMAAzo BCPs were characterized by ¹H NMR and gel permeation chromatography (GPC), Figure 1b,c. ¹H NMR spectra were recorded with a Bruker 400 MHz spectrometer. GPC was conducted on a Waters 1515 instrument with pure THF as eluent (1.0 mL/min). The calibration curve was obtained with linear PSs as standards. GPC provides relative molecular weights, whereas the NMR result is quantitative.

The thermal behavior and LC phase transitions were studied using differential scanning calorimetry (DSC) and polarized optical microscopy (POM, Nikon, ECLIPSE LV100 POL) equipped with a hot stage. The DSC experiment was carried out on a TA Q200 (USA calorimeter) in a nitrogen atmosphere. The heating and cooling rate was 10 °C/min, and the glass transition temperature ($T_{\rm g}$) and LC-isotropic phase transition temperature ($T_{\rm LC-iso}$) of the BCPs were recorded from the second heating curve.

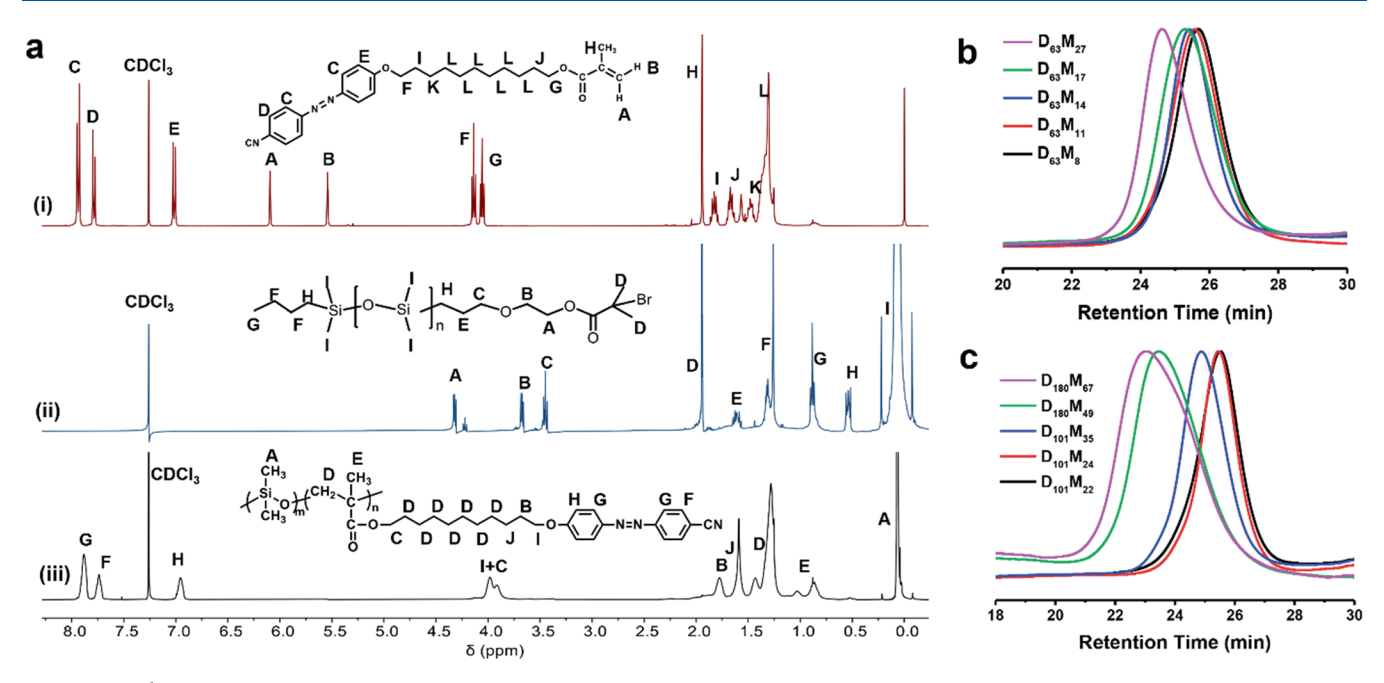


Figure 1. (a) ¹H NMR spectra of (i) MAAzo monomer; (ii) PDMS-Br macroinitiator; and (iii) $D_{63}M_{14}$. Insets show the molecular structures. (b,c) GPC curves of (b) $D_{63}M_{n}$; (c) $D_{101}M_{n}$; and $D_{180}M_{n}$ BCPs.

Table 1. Molecular Weights M_n , Dispersity M_w/M_n , f_{PMAAzo} , Morphology, and q and d Values of the BCPs

sample ^a	$M_{\rm n}^{\ b}$ (g/mol)	$M_{\rm n}^{c}$ (g/mol)	$M_{\rm w}/M_{\rm n}^{}$	$f_{ m PMAAzo}$ (%)	nanostructure	$q^* (nm^{-1})$	d (nm)
$D_{63}M_{8}$	11,300	8300	1.15	41	LAM	0.370	17.0
$D_{63}M_{11}$	12,000	9700	1.18	49	GYR	0.347	18.2
$D_{63}M_{14}$	12,200	11,100	1.13	55	GYR	0.334	18.8
$D_{63}M_{17}$	13,000	12,500	1.17	60	HEX	0.331	19.0
$D_{63}M_{27}$	17,200	17,100	1.18	71	BCC	0.310	20.3
$D_{101}M_{22}$	14,800	17,600	1.15	55	Fddd	0.306	20.5
$D_{101}M_{24}$	14,900	18,500	1.11	57	HEX	0.295	21.3
$D_{101}M_{35}$	18,200	23,600	1.15	66	BCC	0.289	21.7
$D_{180}M_{49}$	25,700	35,900	1.35	60	HEX	0.244	25.7
$D_{180}M_{67}$	28,200	44,200	1.45	67	BCC	0.230	27.3

[&]quot;PDMS-b-PMAAzo is denoted as $D_m M_n$, where m and n are the degrees of polymerization of PDMS blocks and PMAAzo blocks, respectively. **Determined by GPC. **Determined by 1H NMR and the PDMS block, which is also determined from 1H NMR.

The microphase-separated nanostructures and the LC phase structures as well as the phase transitions were characterized by SAXS and wide-angle X-ray scattering (WAXS) experiments. SAXS experiments were carried out on a Xeuss2.0 (Xenocs) instrument and Bruker Nanostar SAXS instrument using Cu K α radiation at a wavelength of 0.154 nm. The working voltage and current were 50 kV and 0.60 mA, respectively. The scattering vector q is defined as $q = 4\pi/\lambda \sin \theta$, where the scattering angle is 2θ , and the d-spacing (d) is given by $2\pi/q$. The WAXS experiments were performed on a Bruker D8 Discover X-ray diffractometer. The X-ray wavelength 0.154 nm from a generator operated at 45 kV and 0.90 mA.

The morphologies of the BCP films were characterized by TEM. BCP films of 50–100 nm thickness were cast on carbon-coated 400-mesh copper grids from a 1.0 wt % solution of BCP in toluene and thermally annealed and then TEM bright field images were obtained with a Talos F200i transmission electron microscope using an accelerating voltage of 120 kV. Due to the higher electron density of PDMS than that of the PMAAzo, the BCP samples were directly observed without staining treatment, ^{27,49} and in the TEM micrographs, the dark part is the PDMS microdomain and the bright part is the PMAAzo microdomain.

The annealed BCP thin films on substrates were subjected to a two-step reactive ion etching (Plasma-Therm 790) consisting of a 50W CF₄ plasma at 15 mTorr for 5 s to remove the PDMS wetting

layer on the surface and a 90W O_2 plasma at 6 mTorr for 10-20 s to selectively etch the PMAAzo matrix, leaving oxidized PDMS microdomains on the substrates. The morphologies of the etched BCP thin films were characterized using a Zeiss Merlin high resolution scanning electron microscopy (SEM) at 3 kV, and with atomic force microscopy (AFM) in both height and phase-contrast modes using a Veeco Metrology Nanoscope V scanned probe microscope controller with a Dimension 3100 AFM in the tapping mode.

3. RESULTS AND DISCUSSION

3.1. Synthesis and Characterization of PDMS-*b*-PMAZO BCPs. The chemical structure and the molecular weights of the three series of PDMS-*b*-PMAAZO diblock copolymers ($D_{63}M_n$, $D_{101}M_n$, and $D_{180}M_n$) are given in Table 1. From the GPC results (Figure 1b,c), the molecular weight distribution of the $D_{63}M_n$ and $D_{101}M_n$ BCPs was narrower than that of the $D_{180}M_n$. Based on the ¹H NMR results and densities of 0.97 g/cm³ for PDMS and 1.10 g/cm³ for PMAAZO, ⁵⁰ the total molecular weight of these BCPs ranged from 8300 to 44,200 g/mol, and the calculated volume fractions of the PMAAZO ranged from 41 to 71%. The f_{PMAAZO} values for

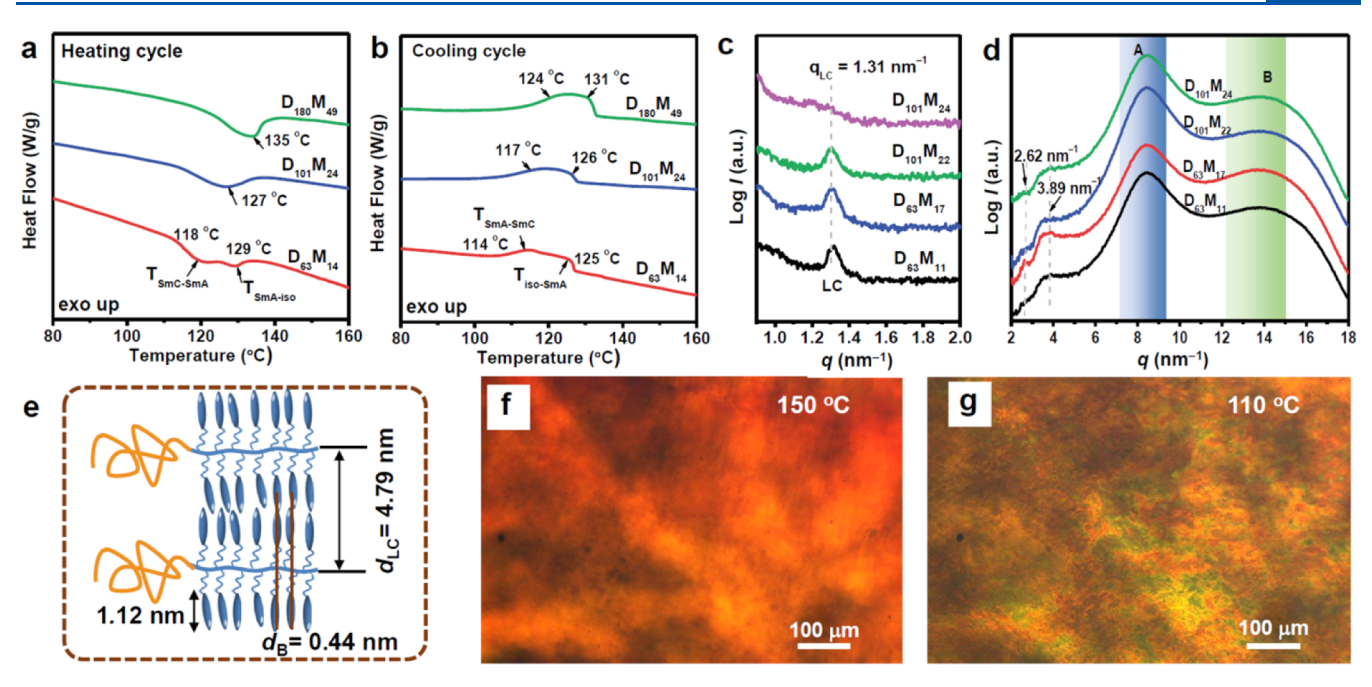


Figure 2. LC behavior of the PMAAzo block. (a,b) DSC curves of $D_{63}M_{14}$, $D_{101}M_{24}$, and $D_{180}M_{49}$ BCPs during the second heating and the first cooling cycle; (c) the SAXS profiles in the wide angle region and (d) 1D WAXS profiles of $D_{63}M_{11}$, $D_{63}M_{17}$, $D_{101}M_{22}$, and $D_{101}M_{24}$; (e) schematic illustration of the bilayer packing of LC mesogens in a SmA LC phase; and the POM images of $D_{63}M_{14}$ at (f) 150 and (g) 110 °C.

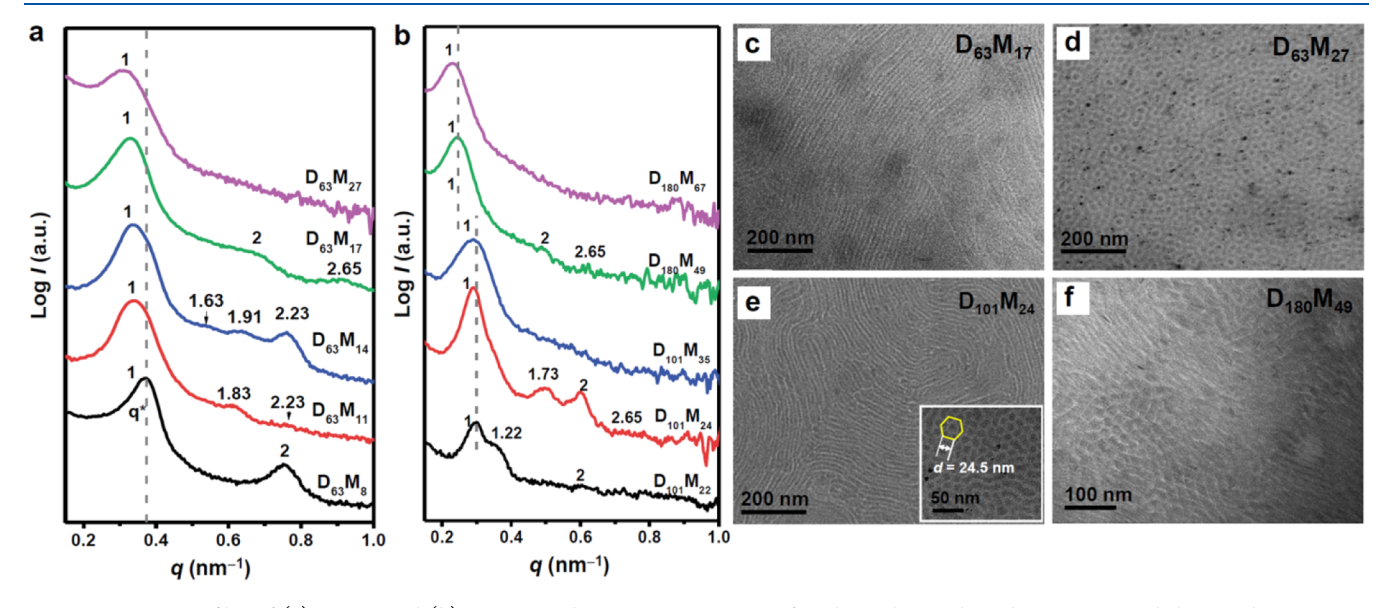


Figure 3. SAXS profiles of (a) $D_{63}M_n$ and (b) $D_{101}M_n$ and $D_{180}M_n$ series BCPs after thermal annealing above $T_{\rm LC-iso}$ and then cooling to room temperature, and TEM images of (c) $D_{63}M_{17}$, (d) $D_{63}M_{27}$, (e) $D_{101}M_{24}$, and (f) $D_{180}M_{49}$ BCPs. In (a), the vertical dashed line represents the primary scattering peak (q^*) of $D_{63}M_8$ and in (b) of $D_{101}M_{22}$ and $D_{180}M_{49}$.

 $D_{63}M_n$, $D_{101}M_n$, and $D_{180}M_n$ cover a similar range, but the molecular weights in each series are different, and thus, these BCPs produce nanostructures with different periods.

3.2. Thermal Properties and LC Phase Behavior of PDMS-b-PMAAzo BCPs. The thermal behavior and mesogen ordering of the PDMS-b-PMAAzo BCPs were investigated using DSC, 1D WAXS, and POM. The DSC curves of all BCPs (Figure S2) indicate both a glass transition and LC phase transition of the PMAAzo block. The glass transition temperature ($T_{\rm g}$), LC transition temperatures, and enthalpy values during the second heating and the first cooling cycles are listed in Table S1. The glass transition was observed in the range of 23–37 °C, and the $T_{\rm g}$ values increased with the

increase in molecular weight of the PMAAzo block.⁵¹ In the heating curve, two distinct endothermic transitions or one broad endothermic transition can be observed in the range of 117–135 °C, which are attributed to LC phase transitions, that is, the smectic C to smectic A phase (SmC–SmA) and the smectic A to the isotropic phase (SmA-I or LC-iso). ⁵² For example, in the enlarged DSC curve of $D_{63}M_{14}$ (Figure 2a), two LC phase transition peaks can be clearly distinguished, and the SmC–SmA and SmA-I occurred at 118 and 129 °C, respectively. The corresponding exothermic peaks can also be observed in the cooling curves corresponding to I-SmA and SmA–SmC transitions (Figures 2b and S2d,h), respectively, and the transition temperatures shift to slightly lower values

due to supercooling. The enthalpy increases with the increase in $f_{\rm PMAAzo}$, and the $T_{\rm LC\text{-}iso}$ increases slightly with an increase of the molecular weight of the PMAAzo. ⁵³

The LC phase and mesogen arrangements of the PMAAzo block of D₆₃M₁₇ and D₁₀₁M₂₄ were further characterized by SAXS and 1D WAXS (Figure 2c,d). In the wide angle region of the SAXS profiles, a scattering peak at $q = 1.31 \text{ nm}^{-1}$ corresponding to a d-spacing of 4.79 nm was observed (Figure 2c). In the small angle region of the 1D WAXS profiles (Figure 2d), two scattering peaks at q = 2.62 and 3.89 nm⁻¹ were observed. These scattering peaks yield a scattering vector ratio of 1:2:3, which indicates that the PMAAzo forms a smectic LC phase. From molecular modeling, the length of the fully extended side group of PMAAzo (Figure S3) was about 2.80 nm and the length of the azobenzene LC mesogen was 1.12 nm (Figure S4). Considering that the methylene group -(CH₂)₁₁- spacers were not in an extended chain conformation, the observed 4.79 nm smectic d-spacing indicates bilayer packing of the LC mesogens (Figure 2e). Two other broad scattering peaks were also observed in the 1D WAXS profiles, in which peak A at $q = 8.59 \text{ nm}^{-1}$, indicating a d-spacing of 0.74 nm, is attributed to the amorphous PDMS block, and peak B at $q = 14.43 \text{ nm}^{-1}$, indicating a d-spacing of 0.44 nm, is attributed to $\pi - \pi$ interactions between azobenzene LC mesogens in the PMAAzo blocks. Moreover, the LC mesogenic texture of the D₆₃M₁₄ BCP was explored by POM. When the $D_{63}M_{14}$ was heated to 150 °C (above the T_{LC-iso} , Figure 2f), the LC block was in an isotropic phase and no texture was observed; when the sample was cooled to 110 °C (Figure 2g), a weak birefringent texture appeared indicating the LC phase formation of the PMAAzo.⁵

3.3. Microphase-Separated Nanostructures of PDMS-b-PMAAzo BCPs in Bulk. We examined the bulk morphologies of all PDMS-b-PMAAzo BCPs by SAXS after thermal annealing above the $T_{\rm LC-iso}$ of the PMAAzo block and cooling to room temperature. The SAXS profiles of $D_{63}M_m$, $D_{101}M_m$, and $D_{180}M_n$ BCPs are shown in Figure 3a,b. TEM observation of bulk samples was limited because the low-molecular-weight BCPs formed sticky solids, which impedes microtome slicing. Instead, we observed the morphologies of solution-cast films by TEM (Figures 3c-f and S6).

We first describe the morphologies of the $D_{63}M_n$ series BCPs after annealing at 150 °C. The SAXS profile of $D_{63}M_8$ with $f_{\rm PMAAzo} \sim 41\%$ presents two scattering peaks with a scattering vector ratio of 1:2 in which the primary scattering peak (q^*) appears at $q=0.370~{\rm nm}^{-1}$ corresponding to a periodicity of 17.0 nm. The cast thin films of $D_{63}M_8$ show a featureless morphology in TEM images (Figure S6a) suggesting a LAM structure parallel to the sample plane.

The SAXS profile of $D_{63}M_{11}$ with $f_{PMAAzo} \sim 49\%$ presents peaks with a scattering vector ratio of 1:1.83:2.23 (Figures 3a and S5 in which the peak at $2.23q^*$ is more obvious). GYR nanostructures produce peaks with ratios $\sqrt{6}:\sqrt{8}:\sqrt{14}:\sqrt{16}:\sqrt{20}:\sqrt{22}:\sqrt{24}:\sqrt{26}:\sqrt{30}:\sqrt{32}...$ with the first two peaks corresponding to the (211) and (220) reflections, respectively. The scattering vector ratio from $D_{63}M_{11}$ is consistent with $\sqrt{6}:\sqrt{20}:\sqrt{30}$ with $q^*=0.347$ nm⁻¹ corresponding to a GYR d-spacing of 18.2 nm. The ratio is inconsistent with that expected from LAM (q ratios 1:2:3...) or HEX $(1:\sqrt{3}:\sqrt{4}:\sqrt{7}:\sqrt{9}:\sqrt{12}...)$, thus a GYR is most likely. However, the TEM image of the cast film showed both featureless regions suggesting parallel LAM and line features suggesting cylinders (e.g., Figure S6b). We conclude that the

cast $D_{63}M_{11}$ film forms a different morphology than that of the SAXS bulk sample as a result of the different confinement conditions.

The SAXS profile of the $D_{63}M_{14}$ sample with $f_{PMAAzo} \sim 55\%$ also shows a series of peaks with the strongest having scattering vector ratios of 1:1.15:1.63:1.91:2.23 consistent with the ratio $\sqrt{6}:\sqrt{8}:\sqrt{16}:\sqrt{22}:\sqrt{30}$ for GYR observed in ref. The peak at $1.15q^*$ is clearer in the data shown in Figure S5. The primary reflection peak at $q=0.334~\rm nm^{-1}$ corresponds to a d-spacing of 18.8 nm. In contrast, the TEM image of the as-cast film presents HEX-dominated nanostructures with a cylinder-to-cylinder distance of 19.3 nm (Figure S6c). The observation of HEX is ascribed to the limited film thickness which promotes the formation of HEX instead of GYR, as seen for $D_{63}M_{11}$.

The SAXS profile of $D_{63}M_{17}$ with $f_{PMAAzo} \sim 60\%$ presents peaks with scattering vector ratio 1:2:2.65, and the primary scattering peak at $q=0.331~{\rm nm}^{-1}$ corresponds to a d-spacing of 19.0 nm in a HEX structure. The formation of HEX was confirmed by the TEM result (Figure 3c) in which the cylinder-to-cylinder distance is 21.2 nm. This is close to the calculated cylinder-to-cylinder distance from the SAXS results of \sim 21.9 nm $(2d/\sqrt{3})$. The radius of the PDMS cylinders is expected to be $d(2f_{\rm PDMS}/\sqrt{3\pi})^{1/2}=7.3~{\rm nm}$.

 $D_{63}M_{27}$ only shows a primary scattering peak in the SAXS profile at $q=0.310~\rm nm^{-1}$, and TEM showed poorly ordered spherical microdomains, corresponding to a BCC structure with a d-spacing value (d_{110}) of $\sim\!20.3~\rm nm$ (Figure 3d). Therefore, we conclude that the $D_{63}M_n$ BCPs produce LAM, GYR, HEX, and BCC nanostructures as the $f_{\rm PMAAzo}$ increased from 41 to 71%, though the GYR structures are inhibited in cast films. The periodicity was less than 22 nm, making them potential candidates for nanolithography applications. 8,57

The SAXS profile of the D₁₀₁M₂₂ presents peaks with a scattering vector ratio of 1:1.22:1.72:1.95, and $q^* = 0.306$ nm^{-1} corresponding to a *d*-spacing of 20.5 nm. The scattering peak at 1.22q* was confirmed by another SAXS instrument (Figure S7) and the peaks at 1.22q* became more clear during in situ heating experiments. The scattering peak at 1.22q* strongly suggests an Fddd morphology. 47 The Fddd structure, an orthorhombic bicontinuous network morphology has been theoretically predicted and experimentally observed as a stable phase in diblock copolymer melts within a narrow region at relatively weak segregation [e.g., for PS-b-polyisoprene (PI) BCPs with $0.629 \le f_{PI} \le 0.649$ and $25 < \chi N < 30$]. Here, the PDMS-b-PMAAzo has a relatively high interaction parameter and low molecular weight, but at the annealing temperature, χ is reduced and this is assumed to promote the Fddd morphology. However, we only observed in-plane cylindrical structures from the TEM image (Figure S6d) indicating that, similar to GYR, the Fddd does not form when the film thickness is smaller than a few times the period of the structure.

 $D_{101}M_{24}$ presents peaks with a scattering vector ratio of 1:1.73:2:2.65, characteristic of HEX, with a primary reflection peak at $q=0.295~\rm nm^{-1}$, corresponding to a d-spacing of 21.3 nm. TEM confirmed the HEX structure with images along and perpendicular to the hexagonal column axis shown in Figure 3e. The SAXS profile of $D_{101}M_{35}$ which had a relatively high dispersity only shows one peak at $q=0.289~\rm nm^{-1}$, corresponding to a d-spacing of 21.7 nm, and the TEM image demonstrates a poorly ordered spherical morphology

(Figure S6e). Thus, we obtained *Fddd*, HEX, and BCC structures from the $D_{101}M_n$ BCPs.

For $D_{180}M_n$ BCPs, TEM of the $D_{180}M_{49}$ showed cylindrical morphology (Figure 3f) and the SAXS was consistent with this, having a scattering vector ratio of 1:2 of the major peaks and a possible third peak at 2.65. The HEX structure with q^* at 0.244 nm⁻¹ corresponds to a d-spacing of 25.7 nm. The cylinder-to-cylinder distance is about 29.7 nm, and the radius of the PDMS cylinders is about 9.8 nm. $D_{180}M_{67}$ only shows one wide primary scattering peak at q=0.230 nm⁻¹ corresponding to a d-spacing value of 27.3 nm, and a poorly ordered spherical morphology was indicated by TEM (Figure S6f). The poor ordering nanostructure of the $D_{180}M_{67}$ should be ascribed to the high dispersity (>1.4) and the higher molecular weight which contributed the lower self-assembly kinetics.

These DM BCPs therefore produce a series of nanostructures with different periodicities. As the $f_{\rm PMAAzo}$ varied from 41 to 71%, LAM, Fddd, GYR, HEX, and BCC structures with different periods were obtained. For approximately constant $f_{\rm PMAAzo}$, the period increased with total molecular weight, while the morphologies were similar. Summarizing the observed morphologies of PDMS-b-PMAAzo BCPs, a schematic phase diagram is illustrated in Figure 4 (χN vs $f_{\rm PMAAzo}$), in which the vertical coordinate χN is proportional to N. The phase boundaries are drawn to correspond to the topology of the phase diagram of ref 59.

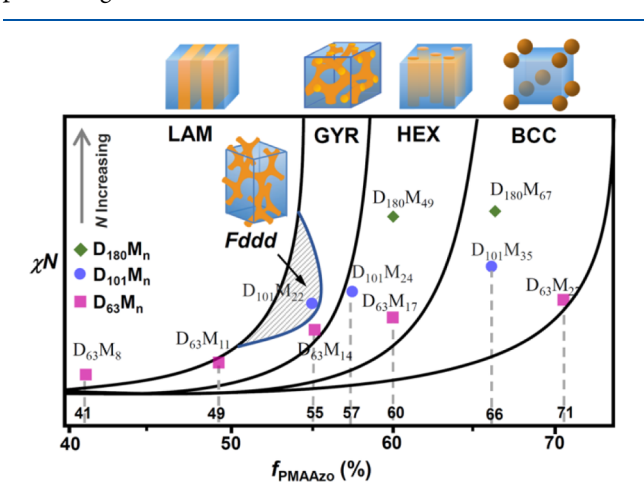


Figure 4. Schematic illustration of the phase diagram, χN vs f_{PMAAzo} of the PDMS-b-PMAAzo BCPs with different total molecular weights.

3.4. Influence of Temperature and LC Phase Transition on Morphology. In Figure S8, we compare the SAXS profiles of the $D_{63}M_{17}$, $D_{101}M_{24}$, and $D_{180}M_{49}$ samples after drying from solution and after thermal annealing, plotting the data from the thermally annealed samples of Figure 3 with that of as-cast samples. The thermally annealed samples presented sharper scattering peaks, and in some cases, the primary scattering peak q^* value was shifted, indicating that the thermal annealing not only highly improved the ordering but also changed the nanostructures.

For LCBCPs, both the LC phase transition of the PMAAzo block and the temperature dependence of χ can influence the microphase separation and order—order transformations of the BCPs. We examined the morphology variation of the D₆₃M₁₄ and D₁₀₁M₂₄ BCPs as a function of temperature using in situ SAXS. In the D₆₃M₁₄ ($f_{\rm PMAAzo} = 55.0\%$), the PMAAzo

exhibited a glass transition at 27 °C and a LC-to-isotropic phase transition at 129 °C. Thermal annealing of D₆₃M₁₄ at 150 °C initially produced a GYR structure that was stable at room temperature, and its subsequent evolution with temperature is shown in Figure 5a. At 100 and 130 °C the first primary scattering peak shifted to a lower q value (0.326 nm $^{-1}$, d-spacing 19.3 nm), but the second scattering peak shifted to a higher q value and its intensity increased. The scattering vector ratio of the peaks changed to 1:1.22:1.67:2, agreeing with that of an Fddd structure. 47,56,60 Within this temperature range, above the $T_{\rm g}$ but below $T_{\rm LC\text{-}iso}$, the PMAAzo block forms a smectic C then a smectic A LC structure. Chain extension maximizes the chain conformational entropy which contributes to the distortion of the GYR structure. When the temperature was increased to 150 and 180 °C, the first primary scattering peak shifted back to higher q values, and the scattering vector ratio changed to 1:1.15:1.73:2, indicating coexistence of the GYR and HEX structures. During the cooling process, the reverse structural transition GYR/HEX-Fddd-GYR was observed from the in situ SAXS results (Figure 5b). The formation of the GYR structure on cooling is attributed to the increase of χ . Therefore, the *Fddd* correlates with the presence of smectic order in the LC block. It is worth noting that incomplete transformation of the structure is likely due to the short annealing time (5 min) at each temperature during the in situ SAXS experiment. However, the structural transitions can clearly be distinguished. We further characterized the nanostructures of the D₆₃M₁₄ after annealing at 120 °C for 48 h and 180 °C for 12 h by room temperature SAXS (Figure S9a,b). The sample annealed at 120 °C presented the characteristic scattering vector ratio of the Fddd structure, and that of the almost GYR structure after being annealed at 180 °C. The results are consistent with the morphology transitions observed in the in situ heating SAXS experiments.

We also observed the phase transitions of D₁₀₁M₂₄ with f_{MAAzo} of 57%, Figure 5c,d. The $D_{101}M_{24}$ exhibited HEX with d-spacing ~21.5 nm at room temperature after thermal annealing at 150 °C. At 100 °C, additional diffraction peaks appeared with the scattering vector ratio 1:1.16:1.22:1.63:1.83:2.24, indicating GYR + Fddd, and the primary peak was at $q = 0.272 \text{ nm}^{-1}$, corresponding to a period of ~23.1 nm. At 130 °C, the Fddd peak is dominant. At 100 and 130 °C, the PMAAzo block adopts a smectic C and smectic A configuration, respectively. When the temperature increased to 150 °C, the primary scattering peak shifted back to a higher q value, and the secondary scattering peaks at 1.16, 1.73, and 2 suggest a HEX + GYR morphology. During the cooling process, the reverse transitions from HEX/GYR to *Fddd* was observed. We further annealed $D_{101}M_{24}$ at 130 °C for 2 days and rapidly quenched it to room temperature. The SAXS profile in Figure S9c shows an improved order, with a larger number of reflection peaks and scattering vector ratios of 1:1.22:1.73:2:2.56:2.74:3.14 which demonstrated a well ordered Fddd structure. 47 Furthermore, D₁₀₁M₂₄ annealed at $180\ ^{\circ}\text{C}$ for 12 h presented scattering vector ratios of 1:1.73:2:3 in SAXS profiles, indicating a well-defined HEX structure (Figure S9d). The in situ WAXS profiles of the $D_{101}M_{24}$ demonstrated the existence of the second order reflection peaks of the smectic phase at 100 and 110 °C, and their absence above 130 °C (Figure S10). According to the DSC and WAXS results, the phase transition and the LC phase transition are correlated.

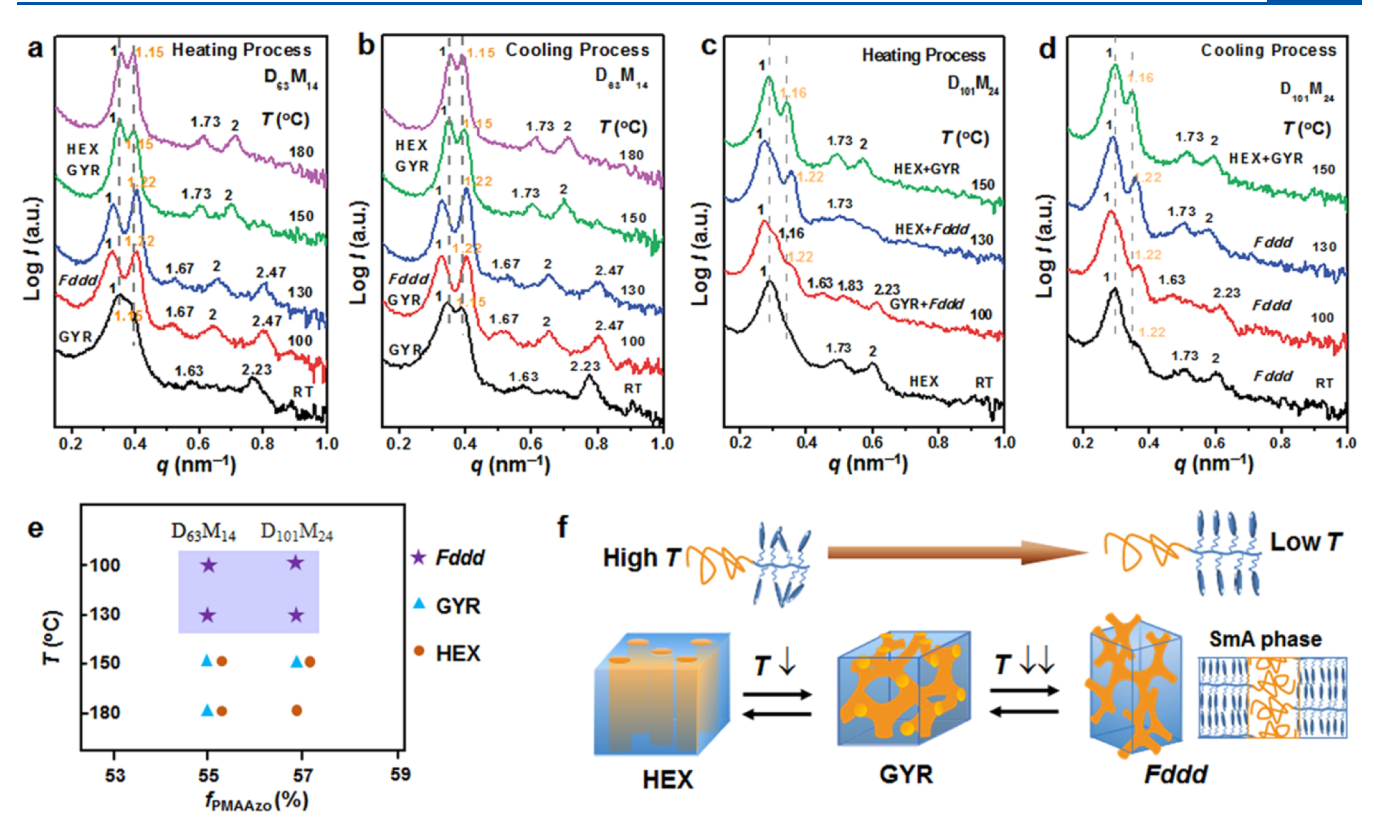


Figure 5. SAXS profiles of (a,b) $D_{63}M_{14}$ and (c,d) $D_{101}M_{24}$ during in situ heating and cooling processes at indicated temperatures. The samples were initially thermally annealed in vacuum at 150 °C for 48 h, measured at RT [curves indicated as RT in (a,c)], then heated to 180 °C with 5 min measurement at each temperature (a,c) and then cooled back to RT (b,d). The vertical dashed lines indicate the position of the primary and second order peaks of the GYR structure and serve as a reference; in the *Fddd* regimes, the peak spacing increases compared to the GYR. (e) The morphologies of $D_{63}M_{14}$ and $D_{101}M_{24}$ formed at different temperatures. (f) Schematic illustration of the HEX-to-GYR-to-*Fddd* transition as well as the LC phase transition of the PMAAzo blocks.

The morphologies of the $D_{63}M_{14}$ and $D_{101}M_{24}$ formed at different temperature are summarized in Figure 5e. The thermally reversible HEX-GYR-Fddd transitions occur as a result of changes in χ and the mesophase-transition of the LC block, schematically illustrated in Figure 5f. The effective χ parameter of the LCBCPs can be expressed as $\chi_{\rm eff} = \chi_{\rm LC} + \chi$, where $\chi \sim 1/T$. The $\chi_{\rm LC}$ contributes to $\chi_{\rm eff}$ when the temperature falls in the range of $T_{\rm g}-T_{\rm LC-iso}$. Above $T_{\rm LC-iso}$, χ is lower ($\chi \sim 1/T$) and $\chi_{\rm LC}$ disappears, so $\chi_{\rm eff}$ is smaller. The GYR structures of $D_{63}M_{14}$ and $D_{101}M_{24}$ with $f_{\rm PMAAzo} \sim$ 55–57% and the PMAAzo in its isotropic phase transform to HEX at a higher temperature induced by the decrease in χ value. However, in the intermediate temperature regime, when the LC block is ordered and $\chi_{\rm eff}$ increased, the Fddd structure forms instead (the temperatures used in this experiment are below the ODT of the BCPs, and even up to 250 °C a disordered structure was not observed).

Prior work has shown that the *Fddd* (orthorhombic O^{70} network) appears in diblock melts within a narrow region of composition and χN that overlaps the weak segregation end of the GYR region 47,61 and thus the *Fddd* is not easily obtained. However, in our PDMS-*b*-PMAAzo BCPs, SAXS data indicated the *Fddd* phase in three different BCPs, in particular when the majority LC block is in a smectic phase. The LC-isotropic phase transition can induce a decrease in the χ value and a possible increase in the apparent volume fraction of the PMAAzo block (the density of the PMAAzo block decreases accompanying the LC-isotropic phase transition), which together contribute to the appearance of *Fddd* phase and

phase transitions of the PDMS-b-PMAAzo BCP with $f_{\rm PMAAzo} \sim 55-57\%$. The LC ordering in PDMS-b-PMAAzo not only promotes microphase separation at low molecular weights but also induces order—order transitions.

3.5. Thin-Film Self-Assembly and Pattern Transfer. The PDMS-*b*-PMAAzo possesses the advantage of a native etch contrast: the PMAAzo block can be removed by oxygen plasma etching leaving ordered silicon oxide (SiO_x) patterns derived from oxidized PDMS. We studied the thin-film self-assembly and pattern transfer of the cylindrical $D_{63}M_{17}$ and $D_{101}M_{24}$ structures by two-step plasma etching, as illustrated in Figure 6a. The $D_{63}M_{17}$ and $D_{101}M_{24}$ thin films with thickness ~40 nm were prepared on bare silicon substrates and annealed at 180 °C for 48 h in vacuum. The annealing temperature is above $T_{\rm LC\text{-iso}}$ and the $D_{63}M_{17}$ and $D_{101}M_{24}$ form cylindrical nanostructures.

Images of a $D_{63}M_{17}$ thin film on bare Si reveal fingerprint patterns from in-plane cylinders (Figure 6b from SEM, Figure 6d from AFM), and the measured cylinder-to-cylinder distance (L_0) is about 20.4 nm which is slightly smaller than that (21.5 nm) of the bulk sample. The $D_{101}M_{24}$ thin film annealed at 180 °C also presented in-plane cylindrical patterns in both SEM and AFM images (Figure 6c,e) and the ordering can be further improved by utilizing a silicon substrate functionalized by a PDMS brush (Figure 6f). The correlation length of the films on the PDMS-functionalized silicon substrate is about $20L_0$, which is much larger than that on the bare silicon substrate $\sim 5L_0$. The distance between the silicon oxide cylinders in $D_{101}M_{24}$ is about 23.8 nm. The preferential in-plane

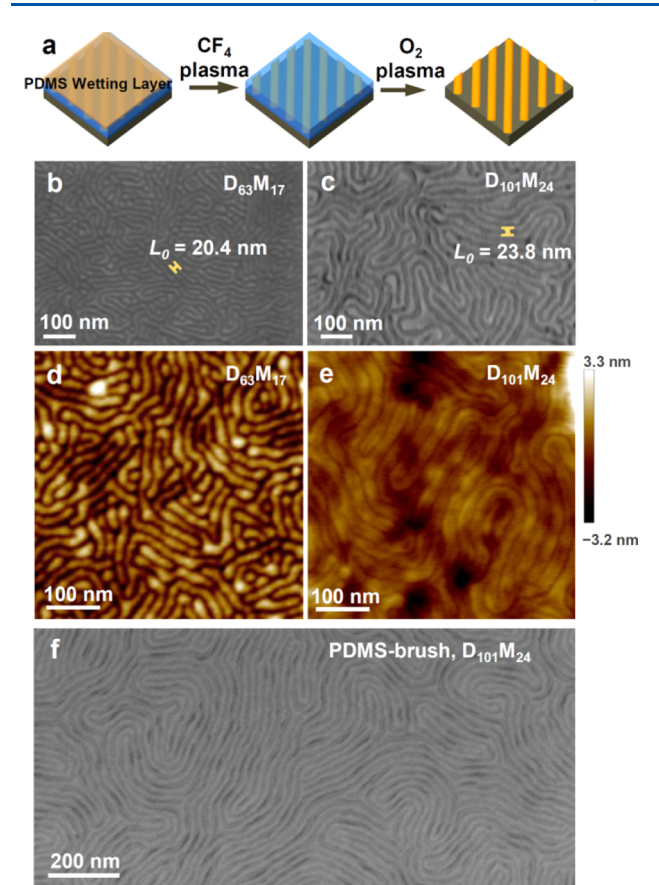


Figure 6. Thin-film morphologies of $D_{63}M_{17}$ and $D_{101}M_{24}$ BCPs after thermal annealing at 180 °C. (a) Schematic illustration of the two-step etching method for pattern transfer; (b,c) SEM images and (d,e) AFM images of the etched thin films on bare silicon substrate; (f) SEM images of $D_{101}M_{24}$ on PDMS brush functionalized silicon substrate.

orientation of the nanostructure is attributed to the wetting behavior of the low-surface energy PDMS block at the interfaces of the BCP films. However, the orientation can be tuned by applying an external field or by taking advantage of the photo-responsive properties of the PMAAzo LC block. 25,37

4. CONCLUSIONS

In summary, we synthesized a series of silicon-containing PDMS-b-PMAAzo azobenzene LC BCPs, and investigated the thermally induced "structure-in-structure" phase transitions as well as the thin-film assembly. The PDMS-b-PMAAzo BCPs with $f_{\rm PMAAzo}$ values ranging from 41 to 71% produced bulk nanostructures of LAM, GYR, Fddd, HEX, and BCC with different periods after annealing at 150 °C. The LC phase behavior of the PMAAzo block correlates with order-order phase transitions of the BCP, and in particular, it appears to favor formation of the Fddd orthorhombic network structure. Thin-film self-assembly of HEX morphology BCPs generated SiO_x nanopatterns by plasma etching in oxygen, which removes the LC block and oxidizes the PDMS block. These azobenzene LC BCPs possess the advantages of native etching contrast and morphology tunability by multiple factors including formation of both Fddd and GYR networks, as well as the potential for orientation switchability by photoillumination demonstrated elsewhere. 23,62 These results

suggest that silicon-containing azobenzene LC BCPs offer useful characteristics for nanopatterning and nanofabrication.

ASSOCIATED CONTENT

Supporting Information

The Supporting Information is available free of charge at https://pubs.acs.org/doi/10.1021/acs.macromol.2c02343.

Materials, synthesis and characterization of the monomer and macroinitiators, GPC curves of $D_{101}M_n$ and $D_{180}M_n$ BCPs, DSC curves of all diblock copolymers, 3D model of the side group and azobenzene group and the bond lengths calculation by Chem 3D software, and additional SAXS and WAXS profiles and TEM images (PDF)

AUTHOR INFORMATION

Corresponding Author

Ling-Ying Shi — College of Polymer Science and Engineering, State Key Laboratory of Polymer Materials Engineering, Sichuan University, Chengdu 610065, China; ⊚ orcid.org/0000-0002-6620-7878; Email: shilingying@scu.edu.cn

Authors

Lin Weng – College of Polymer Science and Engineering, State Key Laboratory of Polymer Materials Engineering, Sichuan University, Chengdu 610065, China

Mingchao Ma – Department of Materials Science and Engineering, Massachusetts Institute of Technology, Cambridge, Massachusetts 02139, United States

Chenxiao Yin — College of Polymer Science and Engineering, State Key Laboratory of Polymer Materials Engineering, Sichuan University, Chengdu 610065, China

Zhi-Xiong Fei — College of Polymer Science and Engineering, State Key Laboratory of Polymer Materials Engineering, Sichuan University, Chengdu 610065, China

Ke-Ke Yang – The Collaborative Innovation Center for Eco-Friendly and Fire-Safety Polymeric Materials (MoE), National Engineering Laboratory of Eco-Friendly Polymeric Materials (Sichuan), College of Chemistry, Sichuan University, Chengdu 610064, China; orcid.org/0000-0002-7019-6059

Caroline A. Ross — Department of Materials Science and Engineering, Massachusetts Institute of Technology, Cambridge, Massachusetts 02139, United States;
orcid.org/0000-0003-2262-1249

Complete contact information is available at: https://pubs.acs.org/10.1021/acs.macromol.2c02343

Notes

The authors declare no competing financial interest.

ACKNOWLEDGMENTS

Financial support from the National Natural Science Foundation of China (grants 52273024), the Applied Basic Research Program of Science and Technology Commission Foundation of Sichuan Province (grants 2021YJ0559), and the Fundamental Research Funds for Central Universities are gratefully acknowledged. C.A.R. and M.M. acknowledge support from the NSF award DMR2118678 and the use of shared facilities of the MIT MRSEC, NSF DMR 1419807.

REFERENCES

- (1) Ahn, H.; Park, S.; Kim, S.-W.; Yoo, P. J.; Ryu, D. Y.; Russell, T. P. Nanoporous Block Copolymer Membranes for Ultrafiltration: A Simple Approach to Size Tunability. *ACS Nano* **2014**, *8*, 11745–11752.
- (2) Jackson, E. A.; Hillmyer, M. A. Nanoporous Membranes Derived from Block Copolymers: From Drug Delivery to Water Filtration. *ACS Nano* **2010**, *4*, 3548–3553.
- (3) Guo, L.; Wang, Y.; Steinhart, M. Porous Block Copolymer Separation Membranes for 21st century sanitation and hygiene. *Chem. Soc. Rev.* **2021**, *50*, 6333–6348.
- (4) Duan, L.; Wang, C.; Zhang, W.; Ma, B.; Deng, Y.; Li, W.; Zhao, D. Interfacial Assembly and Applications of Functional Mesoporous Materials. *Chem. Rev.* **2021**, *121*, 14349–14429.
- (5) Arora, H.; Du, P.; Tan, W.; Hyun, K.; Grazul, J.; Xin, L.; Muller, A.; Thompson, O.; Wiesner, U. Block Copolymer Self-Assembly—Directed Single-Crystal Homo- and Heteroepitaxial Nanostructures. *Science* **2010**, *330*, 214–219.
- (6) Tavakkoli, K. G. A.; Gotrik, K. W.; Hannon, A. F.; Alexander-Katz, A.; Ross, C. A.; Berggren, K. K. Templating Three-Dimensional Self-Assembled Structures in Bilayer Block Copolymer Films. *Science* **2012**, 336, 1294–1298.
- (7) Bates, S. Polymer-Polymer Phase Behavior. Science 1991, 251, 898-905.
- (8) Sinturel, C.; Bates, F. S.; Hillmyer, M. A. High χ -Low N Block Polymers: How Far Can We Go? *ACS Macro Lett.* **2015**, *4*, 1044–1050.
- (9) Lee, J.; Seo, M. Downsizing of Block Polymer-Templated Nanopores to One Nanometer via Hyper-Cross-Linking of High χ -Low N Precursors. *ACS Nano* **2021**, *15*, 9154–9166.
- (10) Hampu, N.; Werber, J. R.; Chan, W. Y.; Feinberg, E. C.; Hillmyer, M. A. Next-Generation Ultrafiltration Membranes Enabled by Block Polymers. *ACS Nano* **2020**, *14*, 16446–16471.
- (11) Lo, T.-Y.; Krishnan, M. R.; Lu, K.-Y.; Ho, R.-M. Silicon-containing Block Copolymers for Lithographic Applications. *Prog. Polym. Sci.* **2018**, *77*, 19–68.
- (12) Cao, H.; Dai, L.; Liu, Y.; Li, X.; Yang, Z.; Deng, H. Methacrylic Block Copolymers Containing Liquid Crystalline and Fluorinated Side Chains Capable of Fast Formation of 4 nm Domains. *Macromolecules* **2020**, *53*, 8757–8764.
- (13) Wang, C.; Li, X.; Deng, H. Synthesis of a Fluoromethacrylate Hydroxystyrene Block Copolymer Capable of Rapidly Forming Sub-5 nm Domains at Low Temperatures. *ACS Macro Lett.* **2019**, *8*, 368–373
- (14) Rho, Y.; Aissou, K.; Mumtaz, M.; Kwon, W.; Pécastaings, G.; Mocuta, C.; Stanecu, S.; Cloutet, E.; Brochon, C.; Fleury, G.; Hadziioannou, G. Laterally Ordered Sub-10 nm Features Obtained From Directed Self-Assembly of Si-Containing Block Copolymer Thin Films. *Small* **2015**, *11*, 6377–6383.
- (15) Jung, Y. S.; Ross, C. A. Orientation-Controlled Self-Assembled Nanolithography Using a Polystyrene–Polydimethylsiloxane Block Copolymer. *Nano Lett.* **2007**, *7*, 2046–2050.
- (16) Tu, K.-H.; Bai, W.; Liontos, G.; Ntetsikas, K.; Avgeropoulos, A.; Ross, C. A. Universal Pattern Transfer Methods for Metal Nanostructures by Block Copolymer Lithography. *Nanotechnology* **2015**, *26*, 375301.
- (17) Chuang, V. P.; Ross, C. A.; Gwyther, J.; Manners, I. Self-Assembled Nanoscale Ring Arrays from a Polystyrene-b-polyferrocenylsilane-b-poly(2-vinylpyridine)Triblock Terpolymer Thin Film. *Adv. Mater.* **2009**, *21*, 3789–3793.
- (18) Huang, M.; Yue, K.; Huang, J.; Liu, C.; Zhou, Z.; Wang, J.; Wu, K.; Shan, W.; Shi, A.-C.; Cheng, S. Z. D. Highly Asymmetric Phase Behaviors of Polyhedral Oligomeric Silsesquioxane-Based Multiheaded Giant Surfactants. *ACS Nano* **2018**, *12*, 1868–1877.
- (19) Lee, S.; Cheng, L.-C.; Gadelrab, K. R.; Ntetsikas, K.; Moschovas, D.; Yager, K. G.; Avgeropoulos, A.; Alexander-Katz, A.; Ross, C. A. Double-Layer Morphologies from a Silicon-Containing ABA Triblock Copolymer. *ACS Nano* **2018**, *12*, 6193–6202.

- (20) Kato, T.; Mizoshita, N.; Kishimoto, K. Functional Liquid-Crystalline Assemblies: Self-Organized Soft Materials. *Angew. Chem., Int. Ed.* **2006**, *45*, 38–68.
- (21) Yu, H.; Kobayashi, T.; Yang, H. Liquid-Crystalline Ordering Helps Block Copolymer Self-Assembly. *Adv. Mater.* **2011**, *23*, 3337–3344.
- (22) Gopinadhan, M.; Choo, Y.; Kawabata, K.; Kaufman, G.; Feng, X.; Di, X.; Rokhlenko, Y.; Mahajan, L. H.; Ndaya, D.; Kasi, R. M.; Osuji, C. O. Controlling Orientational Order in Block Copolymers Using Low-Intensity Magnetic Fields. *Proc. Natl. Acad. Sci. U.S.A.* **2017**, *114*, No. E9437.
- (23) Wang, T.; Li, X.; Dong, Z.; Huang, S.; Yu, H. Vertical Orientation of Nanocylinders in Liquid-Crystalline Block Copolymers Directed by Light. *ACS Appl. Mater. Interfaces* **2017**, *9*, 24864–24872.
- (24) Shi, L.-Y.; Lan, J.; Lee, S.; Cheng, L.-C.; Yager, K. G.; Ross, C. A. Vertical Lamellae Formed by Two-Step Annealing of a Rod—Coil Liquid Crystalline Block Copolymer Thin Film. *ACS Nano* **2020**, *14*, 4289—4297.
- (25) Lee, C.; Osuji, C. O. 100th Anniversary of Macromolecular Science Viewpoint: Opportunities for Liquid Crystal Polymers in Nanopatterning and Beyond. *ACS Macro Lett.* **2021**, *10*, 945–957.
- (26) Liao, F.; Shi, L.-Y.; Cheng, L.-C.; Lee, S.; Ran, R.; Yager, K. G.; Ross, C. A. Self-assembly of a Silicon-Containing Side-Chain Liquid Crystalline Block Copolymer in Bulk and in Thin Films: Kinetic Pathway of a Cylinder to Sphere Transition. *Nanoscale* **2019**, *11*, 285–293.
- (27) Shi, L.-Y.; Hsieh, I. F.; Zhou, Y.; Yu, X.; Tian, H.-J.; Pan, Y.; Fan, X.-H.; Shen, Z. Thermoreversible Order—Order Transition of a Diblock Copolymer Induced by the Unusual Coil—Rod Conformational Change of One Block. *Macromolecules* **2012**, *45*, 9719—9726.
- (28) Guan, Y.; Chen, X.; Ma, H.; Shen, Z.; Wan, X. Order-order transition Induced by Mesophase Formation in a Novel Type of Diblock Copolymers Based on Poly(isobutyl methacrylate) and Poly[2,5-di(isopropyloxycarbonyl)styrene]. *Soft Matter* **2010**, *6*, 922–927
- (29) Shi, L.-Y.; Pan, Y.; Zhang, Q.-K.; Zhou, Y.; Fan, X.-H.; Shen, Z.-H. Synthesis and Self-Assembly of a Linear Coil-Coil-Rod ABC Triblock Copolymer. *Chin. J. Polym. Sci.* **2014**, *32*, 1524–1534.
- (30) Pan, Y.; Shi, L.-Y.; Ping, J.; Zhang, Z.; Gu, K.; Fan, X.-H.; Shen, Z. Thermoreversible Order—Order Transition of a Triblock Copolymer Containing a Mesogen-Jacketed Liquid Crystalline Polymer with a Re-Entrant Phase Behavior. *Macromol. Chem. Phys.* **2016**, 217, 1081—1088.
- (31) Jerca, F. A.; Jerca, V. V.; Hoogenboom, R. Advances and opportunities in the Exciting World of Azobenzenes. *Nat. Rev. Chem.* **2022**, *6*, 51–69.
- (32) Cai, F.; Song, T.; Yang, B.; Lv, X.; Zhang, L.; Yu, H. Enhancement of Solar Thermal Fuel by Microphase Separation and Nanoconfinement of a Block Copolymer. *Chem. Mater.* **2021**, 33, 9750–9759.
- (33) Hu, D.; Chang, X.; Xu, Y.; Yu, Q.; Zhu, Y. Light-Enabled Reversible Shape Transformation of Block Copolymer Particles. *ACS Macro Lett.* **2021**, *10*, 914–920.
- (34) Yu, H.; Iyoda, T.; Ikeda, T. Photoinduced Alignment of Nanocylinders by Supramolecular Cooperative Motions. *J. Am. Chem. Soc.* **2006**, *128*, 11010–11011.
- (35) Morikawa, Y.; Kondo, T.; Nagano, S.; Seki, T. Photoinduced 3D Ordering and Patterning of Microphase-Separated Nanostructure in Polystyrene-Based Block Copolymer. *Chem. Mater.* **2007**, *19*, 1540–1542.
- (36) Morikawa, Y.; Nagano, S.; Watanabe, K.; Kamata, K.; Iyoda, T.; Seki, T. Optical Alignment and Patterning of Nanoscale Microdomains in a Block Copolymer Thin Film. *Adv. Mater.* **2006**, *18*, 883–886.
- (37) Lee, C.; Ndaya, D.; Bosire, R.; Kim, N. K.; Kasi, R. M.; Osuji, C. O. Fast Photoswitchable Order—Disorder Transitions in Liquid-Crystalline Block Co-oligomers. *J. Am. Chem. Soc.* **2022**, *144*, 390–399.

- (38) Aoki, K.; Iwata, T.; Nagano, S.; Seki, T. Light-Directed Anisotropic Reorientation of Mesopatterns in Block Copolymer Monolayers. *Macromol. Chem. Phys.* **2010**, *211*, 2484–2489.
- (39) Wei, R. B.; He, Y. N.; Wang, X. G. Diblock Copolymers Composed of a Liquid Crystalline Azo Block and a Poly-(dimethylsiloxane) Block: Synthesis, Morphology and Photoresponsive Properties. *RSC Adv.* **2014**, *4*, 58386–58396.
- (40) Wang, D.; Ye, G.; Zhu, Y.; Wang, X. Photoinduced Mass-Migration Behavior of Two Amphiphilic Side-Chain Azo Diblock Copolymers with Different Length Flexible Spacers. *Macromolecules* **2009**, *42*, 2651–2657.
- (41) Hong, J.-D.; Jung, B.-D.; Kim, C. H.; Kim, K. Effects of Spacer Chain Lengths on Layered Nanostructures Assembled with Main-Chain Azobenzene Ionenes and Polyelectrolytes. *Macromolecules* **2000**, 33, 7905–7911.
- (42) Weis, P.; Hess, A.; Kircher, G.; Huang, S.; Auernhammer, G. K.; Koynov, K.; Butt, H.-J.; Wu, S. Effects of Spacers on Photoinduced Reversible Solid-to-Liquid Transitions of Azobenzene-Containing Polymers. *Chem.—Eur. J.* **2019**, 25, 10946–10953.
- (43) Xu, Y.-S.; Shi, D.; Gu, J.; Lei, Z.; Xie, H.-L.; Zhao, T.-P.; Yang, S.; Chen, E.-Q. Synthesis and Self-Organization of Azobenzene Containing Hemiphasmidic Side-Chain Liquid Crystalline Polymers with Different Spacer Lengths. *Polym. Chem.* **2016**, *7*, 462–473.
- (44) Bobrovsky, A.; Shibaev, V.; Cigl, M.; Hamplová, V.; Dorovatovskii, P.; Ostrovskii, B.; Bubnov, A. The Effect of Spacer and Alkyl Tail Lengths on the Photoorientation Processes in Amorphousized Films of Azobenzene-Containing Liquid Crystalline Polymethacrylates. *Liq. Cryst.* **2020**, *47*, 377–383.
- (45) Seki, T.; Sakuragi, M.; Kawanishi, Y.; Tamaki, Y.; Fukuda, T.; Ichimura, K.; Suzuki, Y. "Command Surfaces" of Langmuir-Blodgett Films. Photoregulations of Liquid Crystal Alignment by Molecularly Tailored Surface Azobenzene Layers. *Langmuir* 1993, 9, 211–218.
- (46) Shimomura, M.; Ando, R.; Kunitake, T. Orientation and Spectral Characteristics of the Azobenzene Chromophore in the Ammonium Bilayer Assembly. *Ber. Bunsenges. Phys. Chem.* **1983**, 87, 1134–1143.
- (47) Takenaka, M.; Wakada, T.; Akasaka, S.; Nishitsuji, S.; Saijo, K.; Shimizu, H.; Kim, M. I.; Hasegawa, H. Orthorhombic Fddd Network in Diblock Copolymer Melts. *Macromolecules* **2007**, *40*, 4399–4402.
- (48) Shi, L.-Y.; Lee, S.; Du, Q.; Zhou, B.; Weng, L.; Liu, R.; Ross, C. A. Bending Behavior and Directed Self-Assembly of Rod—Coil Block Copolymers. ACS Appl. Mater. Interfaces 2021, 13, 10437—10445.
- (49) Michler, G. H. Electron Microscopy of Polymers; Springer-Verlag: Berlin, 2008.
- (50) Qu, T.; Guan, S.; Zhang, C.; Zheng, X.; Zhao, Y.; Chen, A. Liquid crystalline Moiety-Assisted Perpendicular Orientation of Cylindrical Domains within P4VP-b-PMA(Az) Films with High Aspect Ratio. *Soft Matter* **2018**, *14*, 7107–7112.
- (51) Shi, L.-Y.; Shen, Z.; Fan, X.-H. Order—Order Transition in a Rod—Coil Diblock Copolymer Induced by Supercritical CO2. *Macromolecules* **2011**, *44*, 2900—2907.
- (52) Tian, Y.; Watanabe, K.; Kong, X.; Abe, J.; Iyoda, T. Synthesis, Nanostructures, and Functionality of Amphiphilic Liquid Crystalline Block Copolymers with Azobenzene Moieties. *Macromolecules* **2002**, 35, 3739–3747.
- (53) Mao, G.; Wang, J.; Clingman, S. R.; Ober, C. K.; Chen, J. T.; Thomas, E. L. Molecular Design, Synthesis, and Characterization of Liquid Crystal—Coil Diblock Copolymers with Azobenzene Side Groups. *Macromolecules* **1997**, *30*, 2556—2567.
- (54) Anthamatten, M.; Hammond, P. T. A SAXS Study of Microstructure Ordering Transitions in Liquid Crystalline Side-Chain Diblock Copolymers. *Macromolecules* **1999**, *32*, 8066–8076.
- (55) Vukovic, I.; Voortman, T. P.; Merino, D. H.; Portale, G.; Hiekkataipale, P.; Ruokolainen, J.; ten Brinke, G.; Loos, K. Double Gyroid Network Morphology in Supramolecular Diblock Copolymer Complexes. *Macromolecules* **2012**, *45*, 3503–3512.
- (56) Shi, L.-Y.; Zhou, Y.; Fan, X.-H.; Shen, Z. Remarkably Rich Variety of Nanostructures and Order–Order Transitions in a Rod–Coil Diblock Copolymer. *Macromolecules* **2013**, *46*, 5308–5316.

- (57) Bates, C. M.; Bates, F. S. 50th Anniversary Perspective: Block Polymers—Pure Potential. *Macromolecules* **2017**, *50*, 3–22.
- (58) Kim, M. I.; Wakada, T.; Akasaka, S.; Nishitsuji, S.; Saijo, K.; Hasegawa, H.; Ito, K.; Takenaka, M. Determination of the Fddd Phase Boundary in Polystyrene-block-polyisoprene Diblock Copolymer Melts. *Macromolecules* **2009**, 42, 5266–5271.
- (59) Tyler, C. A.; Morse, D. C. Orthorhombic \$Fddd\$ Network in Triblock and Diblock Copolymer Melts. *Phys. Rev. Lett.* **2005**, *94*, 208302.
- (60) Wang, Y.-C.; Kim, M. I.; Akasaka, S.; Saijo, K.; Hasegawa, H.; Hikima, T.; Takenaka, M. Fddd Structure in Polystyrene-block-polyisoprene Diblock Copolymer/Polystyrene Homopolymer Blends. *Macromolecules* **2016**, 49, 2257–2261.
- (61) Kim, M. I.; Wakada, T.; Akasaka, S.; Nishitsuji, S.; Saijo, K.; Hasegawa, H.; Ito, K.; Takenaka, M. Stability of the Fddd Phase in Diblock Copolymer Melts. *Macromolecules* **2008**, 41, 7667–7670.
- (62) Nickmans, K.; Bögels, M.; Sánchez-Somolinos, C.; Murphy, N.; Leclère, P.; Voets, K.; Schenning, P. H. J. 3D Orientational Control in Self-Assembled Thin Films with Sub-5 nm Features by Light. *Small* **2017**, *13*, 1701043.

☐ Recommended by ACS

Self-Assembly of Gyroid-Forming Diblock Copolymers under Spherical Confinement

Yen-Ting Juan, Han-Yu Hsueh, et al.

JANUARY 10, 2023 MACROMOLECULES

READ 🗹

Selective Swelling of Polystyrene (PS)/Poly(dimethylsiloxane) (PDMS) Block Copolymers in Alkanes

Shoutian Qiu, Yong Wang, et al.

DECEMBER 26, 2022

MACROMOLECULES

READ 🗹

Accessing the Frank–Kasper σ Phase of Block Copolymer with Small Conformational Asymmetry via Selective Solvent Solubilization in the Micellar Corona

Meng-Zhe Chen, Hsin-Lung Chen, et al.

DECEMBER 08, 2022 MACROMOLECULES

READ 🗹

Nanospheres with Patches Arranged in Polyhedrons from Self-Assembly of Solution-State Diblock Copolymers under Spherical Confinement

Jiaping Wu, Baohui Li, et al.

DECEMBER 29, 2022

MACROMOLECULES

READ 🗹

Get More Suggestions >